coatings

Article

Analysis of Interlayer Crack Propagation and Strength Prediction of Steel Bridge Deck Asphalt Pavement Based on Extended Finite Element Method and Cohesive Zone Model (XFEM–CZM) Coupling

Chen Zhu, Weiwei Li and Hongchang Wang *

College of Civil Engineering, Nanjing Forestry University, Nanjing 210037, China; zhuchenupup@126.com (C.Z.); m17367077658@163.com (W.L.)
* Correspondence: seuwhc@126.com

Abstract: The extended finite element method (XFEM) was employed for the computational modeling of internal defects within a bond layer. Furthermore, a cohesive zone model (CZM) was implemented to characterize the behavior of the bond layer in response to interactions at both the bond layer/steel plate and bond layer/asphalt paving layer interfaces. The coupling of XFEM and CZM was used for a comprehensive analysis of crack propagation within the bond layer as well as the assessment of phenomena associated with interfacial debonding and delamination. The feasibility and accuracy of the XFEM–CZM coupling method were verified by comparing it with the virtual crack closure technique (VCCT), CZM, XFEM–VCCT, and experiments. A double cantilever beam experimental model was established to simulate the process of interlayer-type cracks expanding from the inside of the bond layer to the interface between the bond layer and the upper and lower layers, causing debonding. This was undertaken to analyze the damage failure mechanism of interlayer-type cracks in asphalt paving layers of steel bridge decks; to discuss the impacts of the initial crack length, the interface stiffness, the interface strength, and the thickness of the bond layer on the performance of the overall interlayer bond strength; and to carry out the significance analysis. The results showed that the initial crack length, interface stiffness, and bond layer thickness had different effects on the expansion path of interlayer cracks. The interlayer strength decreased with an increase in the initial crack length and interface stiffness, increased with an increase in the interface strength, and decreased with an increase in the thickness of the bond layer. The interface stiffness had the most significant effect on the strength.

Keywords: steel bridge deck pavement; interlayer crack; extended finite element method (XFEM); cohesion zone model (CZM); interface debonding

Citation: Zhu, C.; Li, W.; Wang, H. Analysis of Interlayer Crack Propagation and Strength Prediction of Steel Bridge Deck Asphalt Pavement Based on Extended Finite Element Method and Cohesive Zone Model (XFEM–CZM) Coupling. *Coatings* **2023**, *13*, 1973. https://doi.org/10.3390/coatings13111973

Academic Editors: Bohayra Mortazavi and Valeria Vignali

Received: 14 October 2023
Revised: 18 November 2023
Accepted: 18 November 2023
Published: 20 November 2023

1. Introduction

Asphalt pavement layers are extensively used to surface large-span steel bridge decks [1]. These asphalt layers endure harsh environmental conditions, experiencing prolonged exposure to fluctuating traffic loads as well as the combined effects of temperature and rainfall. These factors create complex composite actions, often resulting in distresses such as rutting, accumulation, and cracking [2,3]. Consequently, the adhesive behavior between the asphalt pavement layers and the steel bridge deck panels becomes notably intricate [4] and interlayer damage readily occurs in such complex settings. Simultaneously, during the paving process, high temperatures generate residual stresses within the bonding layer [5], diminishing its adhesive strength and eventually leading to delamination between the steel bridge deck panels and the asphalt pavement layer. Cracks emerging from this delamination rapidly propagate, causing the breakdown of the entire bonding layer. In this scenario, the load cannot effectively be transmitted to the steel bridge deck panels, resulting in a reduction in the overall strength of the pavement system.

The structural configuration of a steel bridge deck pavement represents a classic stratified composition, typically consisting of a pavement layer, waterproof bonding layer, and steel bridge deck (as illustrated in Figure 1) [6]. Extensive research has been dedicated to investigating interlayer bonding within steel bridge deck pavements. This research has revealed that due to material performance disparities and construction process deficiencies, inadequate interlayer bonding is a common issue, resulting in a diminished load-carrying capacity between layers [7–11]. Unlike road pavements, bridge deck pavements experience distinctive stress conditions, environmental factors, and usage circumstances, making them more susceptible to a variety of distresses. The performance of the pavement directly affects the durability, safety, and driving comfort of bridges [12].

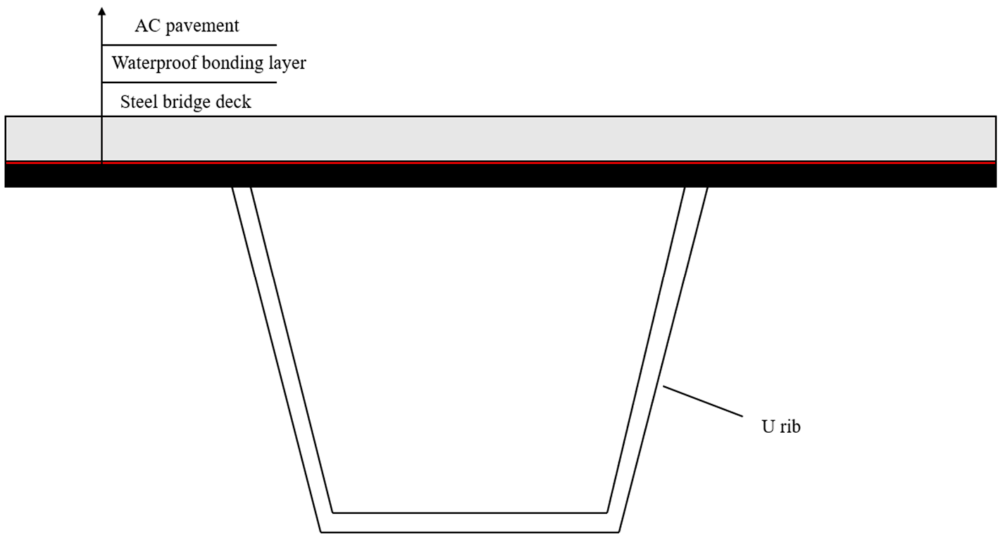

Figure 1. Typical composite structure of SBDP.

Previous research on the interlayer bonding of steel bridge deck pavements has mainly considered factors such as the adhesive material type and quantity, interface roughness, and external factors like environmental conditions, temperature, and loads [13–16]. Chen and others [17] evaluated the interactive effects of factors such as voids in asphalt concrete pavement, the roughness of steel bridge deck surfaces, the thickness of zinc-rich epoxy primers, and waterproof bonding membranes on pavement bonding strength through load simulations. They concluded that optimizing the design of steel bridge deck pavement structures requires a multifactor approach. Yang Liu and colleagues [18] analyzed residual stresses between steel bridge deck asphalt pavement layers and steel plates, noting that significant residual stresses could lead to interlayer cracking initiation, ultimately causing interlayer bonding failure. Graczyk and coauthors [19] employed numerical analysis models to construct a structural model of bridge deck pavement layers, investigating interlayer stress and deformation states under varying climatic and load conditions. They further elucidated the mechanism of interlayer bonding failure due to gas accumulation forming bubbles between asphalt concrete and bridge deck panels, proposing preventive measures. Nie and collaborators [20] researched the impact of the watertightness of epoxy asphalt mixtures on the bonding performance of steel plate interfaces. They discovered that epoxy asphalt concrete exhibits notable watertightness, protecting steel plate interfaces from corrosion and ensuring robust bonding performance. Yuya and others [21] analyzed the effect of interlayer bonding on the deterioration of asphalt pavements and clarified the importance of interlayer bonding.

However, limited attention has been given to the mechanisms of interlayer crack propagation. Fracture mechanics and damage mechanics serve as effective tools in simulating stratified composite materials [22,23]. Within fracture mechanics, crack propagation can be categorized into three types: opening mode (Mode I), sliding mode (Mode II), and tearing mode (Mode III). Combinations of these three modes form mixed-mode cracks. Analyzing the propagation mechanisms of each distinct type of crack can provide deeper insights into composite crack propagation mechanisms. This study primarily focuses on investigating the expansion of Mode I interlayer cracks.

In recent years, the application of numerical simulations in engineering has become increasingly common [24] and the coupled XFEM–CZM (extended finite element method–cohesive zone model) approach has emerged as a robust tool to characterize interlayer bonding failure patterns in composite materials [25]. However, the majority of related investigations have predominantly focused on adhesive joints [26], thus exhibiting limitations in their scope. Furthermore, a comparative analysis involving other interface delamination methods such as VCCT (virtual crack closure technique), CZM, and XFEM–VCCT is notably absent. The steel bridge deck pavement system can effectively be conceptualized as an adhesive system, with the bonding layer akin to an adhesive layer. This study proposes the application of the XFEM–CZM coupling technique to scrutinize the propagation of Mode I interlayer cracks and predict their strength within steel bridge deck asphalt pavement layers.

2. Numerical Methods and Damage Models

2.1. XFEM

The extended finite element method (XFEM) is a sophisticated numerical approach to address fracture mechanics challenges and was initially proposed in 1999 [27,28]. Over more than two decades of refinement, this method has demonstrated its efficacy in analyzing problems involving discontinuities in mechanics. When tackling crack propagation, XFEM stands out due to its unique characteristics: it obviates the need to account for the crack interface, eliminates the necessity for an intricately detailed mesh near the crack tip's stress singularity zone, and avoids the requirement to remesh during crack extensions. As a result, XFEM has emerged as a highly advantageous solution to crack expansion issues.

XFEM is built upon the concept of unit decomposition [29–31], enhanced by the introduction of enrichment functions that facilitate a specific representation of discontinuous displacements. This innovation allows for the independent existence of cracks and meshes, as depicted in Figure 2.

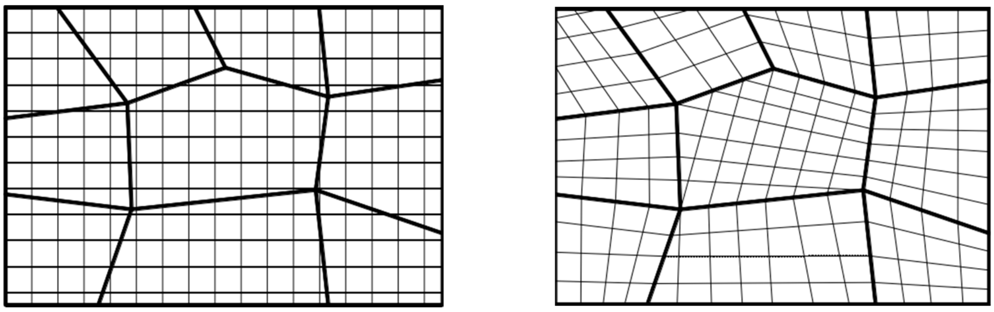

(**a**) XFEM (**b**) FEM

Figure 2. A comparison between traditional finite element and extended finite element meshing.

The approximated displacement field within the solution domain is formulated as follows:

$$u = \sum_{i \in N} N_i(x) u_i + \sum_{j \in N^{cut}} N_j(x) H(x) a_j + \sum_{k \in N^{asy}} N_k(x) \sum_{\propto=1}^{4} F_{\propto}(x) b_k^{\propto} \quad (1)$$

where N represents the set of all regular unit nodes, N^{cut} signifies the set of unit nodes fully intersected by cracks, and N^{asy} denotes the set of unit nodes around the crack tips. $N_i(x)$, $N_j(x)$, and $N_k(x)$ are the shape functions of the corresponding nodes, while $H(x)$ is the discontinuous jump function across the crack surface. This function can be represented using the Heaviside function:

$$H(x) = \begin{cases} 1 \ (x - x^*) \cdot n \geq 0 \\ -1 \quad n < 0 \end{cases} \tag{2}$$

Here, x represents the Gaussian sample point, x^* is the point nearest to x on the crack, and n is the unit outward of the normal vector.

In XFEM, the evolution of crack surfaces and their advancement during expansion are traced through the level set function. This function effectively distinguishes the units penetrated by cracks from those unaffected, enabling the comprehensive tracking of the entire crack expansion process.

2.2. Crack Initiation Criterion and Expansion Criterion of the Bonded Layer

In this paper, the crack expansion inside the bonded layer is analyzed by XFEM, based on Abaqus finite element software. The maximum principal stress criterion is used as the crack initiation criterion within the bonded layer.

$$f = \frac{\langle \sigma_{max} \rangle}{\sigma_{max}^0} \tag{3}$$

where σ_{max} denotes the maximum principal stress and $\langle \ \rangle$ represents the Macaulay operator, indicating that no new cracks form under compressive loads. σ_{max}^0 stands for the maximum allowable stress.

Upon f reaching 1, crack propagation commences, marking the onset of material damage evolution. This paper employs the energy-based power law rule as the damage evolution criterion within the XFEM region:

$$\left\{ \frac{G_I}{G_{IC}} \right\} + \left\{ \frac{G_{II}}{G_{IIC}} \right\} + \left\{ \frac{G_{III}}{G_{IIIC}} \right\} = 1 \tag{4}$$

Here, G_I, G_{II}, and G_{III} represent the strain energy release rates for Type I, II, and III cracks within the bonded layer, respectively. G_{IC}, G_{IIC}, and G_{IIIC} stand for the critical strain energy release rates within the bonded layer. A damage variable is introduced to ascertain the overall damage level of the unit containing the crack, with values ranging from 0 (no damage) to 1 (complete cracking of the enriched unit).

2.3. Interface Damage Model

In this paper, cohesive cells are used to simulate the interface delamination between the asphalt pavement/bonding layer and steel bridge panel/bonding layer. The interface bilinear traction–separation principal structure is shown in Figure 3. In the figure, $t_{n,s,t}^0$ represents the cohesive strength in this context. Subsequently, the material undergoes softening behavior, wherein the interface stiffness of the cohesive zone starts to decrease and the extent of reduction is determined by the damage factor. $k_{nn,ss,tt}$ is the interface stiffness, D is the damage factor, $s_{n,s,t}^0$ is the failure displacement, and $s_{n,s,t}^f$ is the final cracking displacement.

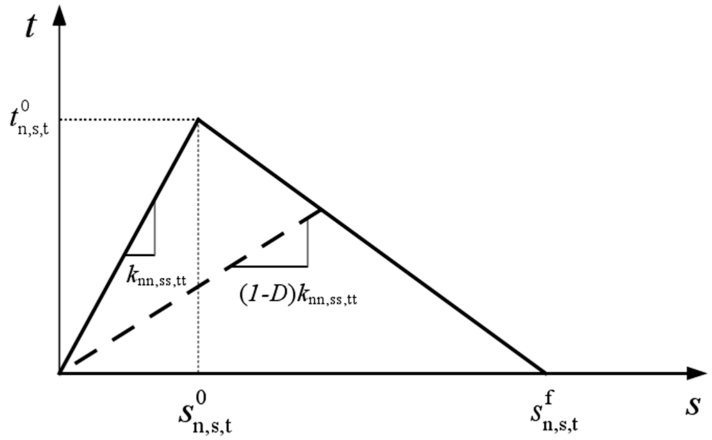

Figure 3. Bilinear traction–separation model of the interface.

(1) Injury initiation criterion

The initiation of damage signifies the material's onset of softening. This process commences when stress or strain meets the specified damage initiation criterion. In this paper, the maximum nominal stress criterion is employed, where damage initiation occurs when any of the nominal stress ratios reach 1:

$$f = max\left\{\frac{\langle t_n \rangle}{t_n^0}, \frac{t_s}{t_s^0}, \frac{t_t}{t_t^0}\right\} \tag{5}$$

Here, t_n denotes the normal force, t_s and t_t indicate the tangential forces, and t_n^0, t_s^0, and t_t^0 represent the normal and tangential forces.

(2) Damage evolution

The evolution of interface damage is governed by the power law equation in this paper:

$$\left\{\frac{G_n}{G_n^C}\right\}^{\alpha} + \left\{\frac{G_s}{G_s^C}\right\}^{\alpha} + \left\{\frac{G_t}{G_t^C}\right\}^{\alpha} = 1 \tag{6}$$

where G_n, G_s, and G_t denote the normal, tangential, and transverse fracture energies, respectively, and G_n^C, G_s^C, and G_t^C are the corresponding critical fracture energies. Equations (7)–(9) describe the cohesive unit's softening behavior:

$$t_n = \begin{cases} (1-D)t_n^0, & t_n^o \geq 0 \\ t_n^0, & t_n^o < 0 \end{cases} \tag{7}$$

$$t_s = (1-D)t_s^0 \tag{8}$$

$$t_t = (1-D)t_t^0 \tag{9}$$

Here, D represents the damage variable, with 0 indicating an undamaged state.

3. Experimental Interlayer Model of a Double Cantilever Beam with a Steel Deck Asphalt Pavement

3.1. Experimental Design of Double Cantilever Beam

The study of Type I cracks commonly employs double cantilevered beam (DCB) specimens [32]. The DCB specimen we used had a length of 0.8 m, a width of 0.35 m, and an initial crack length set at 0.2 m. To ensure that the DCB specimen experienced a vertical upward force, a hinged loading configuration was adopted, with the hinge placed inversely at the specimen's ends to reduce the influence of hinge rigidity on the results.

The entire experiment was conducted on a CMT4202 electronic universal testing machine (The equipment was sourced from Shenzhen Chu Yinghao Technology Co., Ltd., Shenzhen, China). The testing procedure followed a displacement-controlled method, with a loading rate of 0.5 mm/min. Load and displacement measurements were automatically collected through the built-in sensors of the testing machine, allowing the real-time monitoring of load and displacement. To facilitate the observation of crack propagation, white paint was applied on both sides of the crack tip before the experiment.

3.1.1. Specimen Design

In composite structures composed of steel plates and asphalt concrete, it is imperative that the bending stiffness of both the AC structural layer and the steel plate are equivalent. The bending stiffness is the product of the elastic modulus E and the moment of inertia I of the beam section about the neutral axis [33]. The bending stiffness of the AC layer is calculated using Equation (10):

$$D^A = \frac{b_A E_A h_A^3}{12} \tag{10}$$

where D^A denotes the bending stiffness of the AC layer, b_A is the width of the AC layer, E_A is the elastic modulus of the AC layer, and h_A is the thickness of the AC layer.

The bending stiffness of the steel plate structural layer is expressed as:

$$D^s = \frac{b_S E_S h_S^3}{12} \tag{11}$$

where D^s represents the bending stiffness of the steel plate structural layer, b_A is the width of the steel plate structural layer, E_S is the elastic modulus of the steel plate structural layer, and h_S is the thickness of the steel plate structural layer.

For composite beams, the widths of the various structural layers are equal, thus:

$$b_A = b_S \tag{12}$$

By equating D^A and D^s, the ratio of thicknesses between the two structural layers is determined as:

$$\frac{h_A}{h_S} = \sqrt[3]{\frac{E_S}{E_A}} \tag{13}$$

The thickness of the steel plate in our experiment was designed to be 0.014 m, with an elastic modulus of 210,000 MPa. Consequently, the asphalt layer's thickness was computed as 0.066 m. A crack with a length of 0.2 m (where L1 represents the crack length) was prefabricated at the midpoint of the left end of the specimen, as illustrated in Figure 4. The specimen dimensions (where L represents the length of the specimen) are presented in Table 1.

Table 1. Test piece size.

Materials	Length/m	Width/m	Thickness/m
AC	0.8	0.35	0.066
Q345qD	0.8	0.35	0.014

3.1.2. Test Piece Fabrication Method

A prefabricated crack was generated by placing a thin layer of adhesive tape between the steel plate and the AC layer. The adhesive mixture was formulated in a 2:1 ratio of epoxy resin to curing agent. After thorough and uniform mixing, the adhesive was evenly applied to the surface of the steel plate, excluding the areas covered by the tape. Following a 30 min interval, the steel plate was positioned within the mold. Subsequently, the AC was poured over the plate and left undisturbed indoors until demolding.

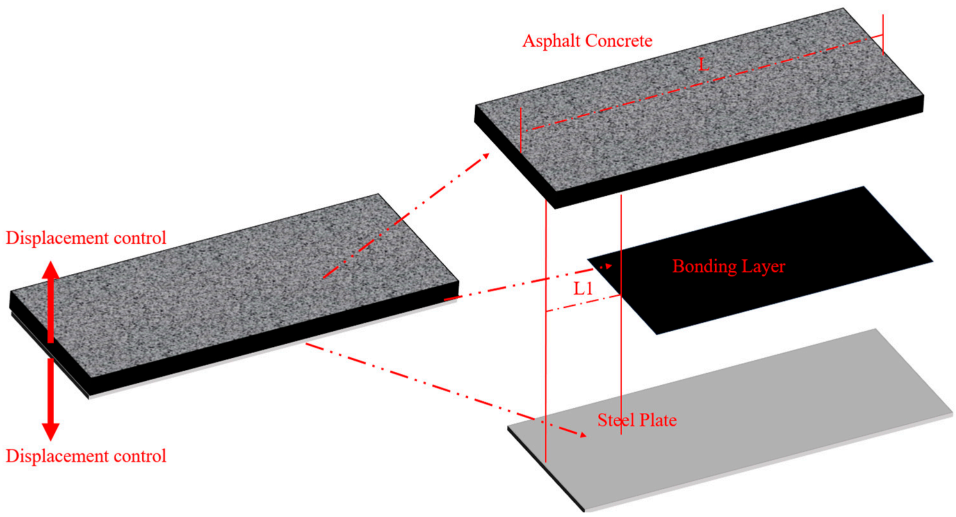

Figure 4. Geometry.

3.2. Finite Element Model

The finite element model of a double cantilever beam (DCB) comprises the AC layer, steel plate, and adhesive layer. The AC layer, steel plate, and adhesive layer in this study were modeled using plane strain elements (CPE4), with the adhesive layer's interior specified as an XFEM region. Interface modeling for the steel bridge deck/adhesive layer and adhesive layer/asphalt pavement layer was accomplished using four-node two-dimensional cohesive elements (COH2D4). The adhesive layer was bias-refined along the longitudinal direction, focusing on the crack propagation region. To accurately represent delamination, the maximum stiffness reduction ratio was set to 0.99, meaning that elements were removed when the damage ratio reached 0.99. Cohesive elements tied the upper and lower layers to the adhesive layer. The choice of the viscosity coefficient affected the model convergence, computational time, and accuracy. This study employed a viscosity coefficient of 1×10^{-5}, significantly improving the model convergence without substantial impacts on the strength and crack propagation predictions. The finite element model is illustrated in Figure 5.

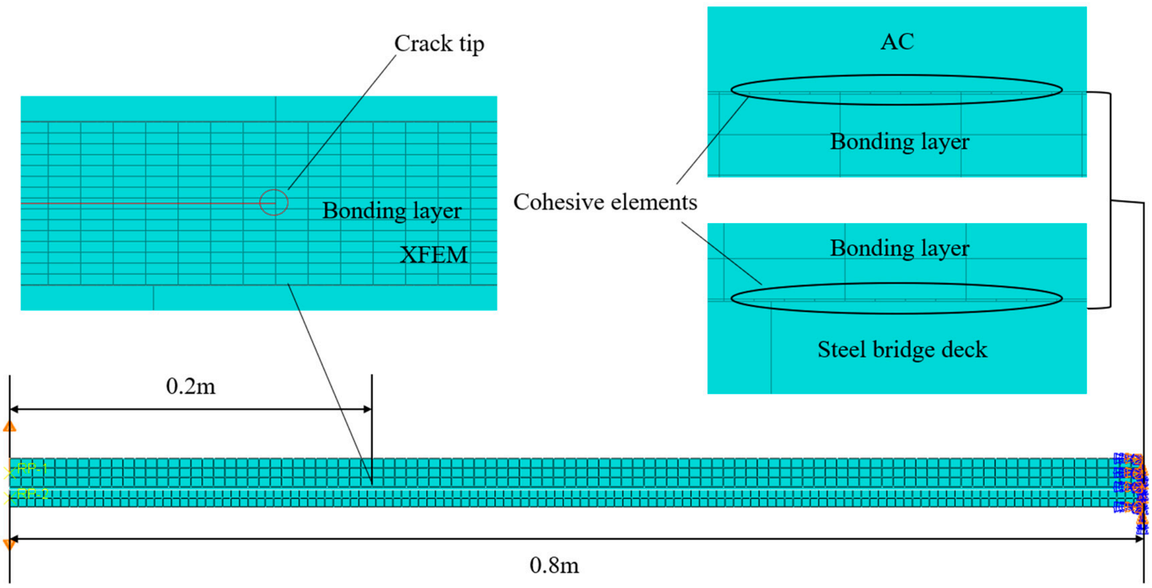

Figure 5. Finite element model.

Tensile and shear strengths were experimentally determined, as depicted in Figure 6. The most unfavorable conditions were chosen. Additionally, as the adhesive layer is inherently thin in practical scenarios, the fracture parameters for the adhesive layer's interior matched those of the interface. Fracture energy was obtained by calculating the area under the load–displacement curve. Interface stiffness was determined by the slope of the load–displacement curve's rising linear segment. The material and interface parameters are specified in Tables 2 and 3, respectively.

(**a**) Tensile test

(**b**) Shear test

Figure 6. Determination of tensile and shear strengths.

Table 2. Material parameters.

Parameters	Steel Plate	AC Layer	Bonding Layer
E/MPa	210,000	4500	100 [34]
v	0.3	0.25	0.25
σ_f/MPa			0.8
τ_f/MPa			0.5
$G_{IC}/\left(\mathrm{J{\cdot}m^{-2}}\right)$			233
$G_{IIC}/\left(\mathrm{J{\cdot}m^{-2}}\right)$			142

E —modulus of elasticity; v —Poisson's ratio; σ_f —normal strength; τ_f —tangential strength.

Table 3. Interface performance parameters.

Interface Parameters	Numerical Value
$K/\left(\mathrm{N{\cdot}mm^{-3}}\right)$	5.069×10^{11}
N/MPa	0.8
$S = T/\mathrm{MPa}$	0.5
$G_{IC}/\left(\mathrm{J{\cdot}m^{-2}}\right)$	233
$G_{IIC} = G_{IIIC}/\left(\mathrm{J{\cdot}m^{-2}}\right)$	142

It is worth noting that in our study, to simplify the model for ease of analysis, we made certain assumptions and simplifications. We chose to consider conditions under a constant temperature and the materials were assumed to be linear elastic, which may have certain limitations [25,34]. Nevertheless, it is important to emphasize that the adoption of these simplifications was aimed at ensuring the feasibility of the model and the clarity of the results. We believed that these simplifications made our models easier to understand and applicable to some actual engineering problems.

4. Numerical Validation and Parameter Discussion

4.1. Numerical Verification

Various mesh quantities were considered to assess their impact on the predicted outcomes. This study anticipated the maximum load and corresponding displacement associated with the extension of Type I cracks between a steel bridge deck's asphalt paving layers for different element counts in the adhesive layer. The adhesive layer's element counts were set at 50,000, 65,000, 70,000, 75,000, 85,000, and 95,000. Corresponding predictive data are detailed in Table 4. Evidently, as the adhesive layer's element count exceeded 70,000, the element density's effect on the adhesive layer strength diminished. This study opted for 75,000 elements to both ensure computational accuracy and reduce the processing time.

Table 4. Influence of element count on load–displacement prediction results for Type I cracks between asphalt paving layers of a steel bridge deck.

Element Count	Maximum Load/N	Displacement/mm
50,000	6248.321	0.688
65,000	5882.212	0.656
70,000	5652.465	0.628
75,000	5544.823	0.629
85,000	5642.330	0.629
95,000	5598.426	0.631

To validate the method employed in this study, four different Type I crack propagation models—VCCT, CZM, XFEM–CZM, and XFEM–VCCT—were established, as illustrated in Figure 7. A comparison was performed using the load–displacement curves obtained from the double cantilever beam (DCB) experiment. Figure 8 illustrates the load–displacement curves of the DCB under the influence of the different methods.

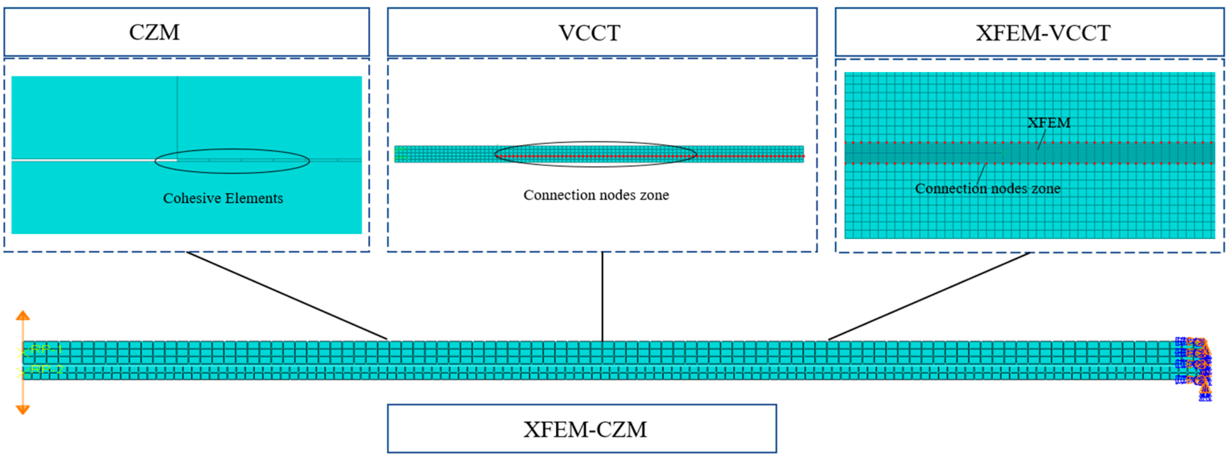

Figure 7. Comparison of methods.

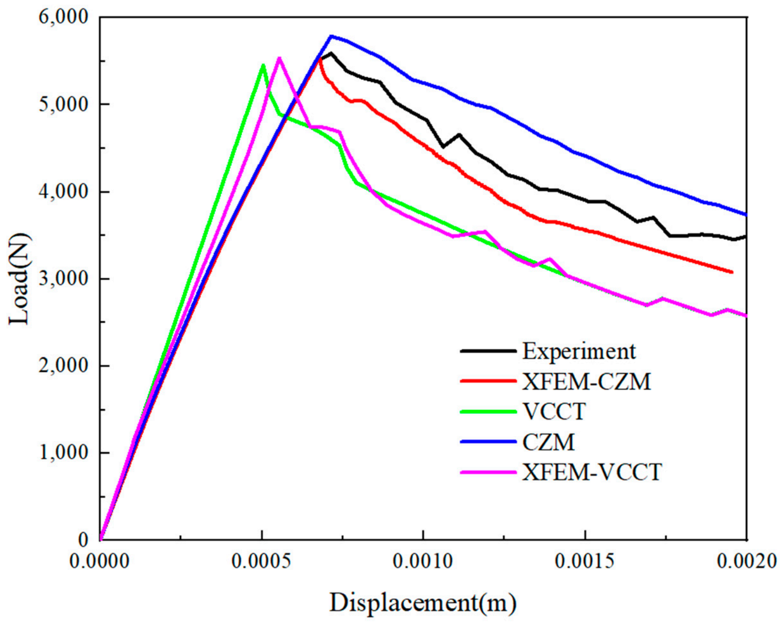

Figure 8. Load–displacement curves of DCB with different methods.

During the ascending phase of the curve, the internal defects (initial crack) within the adhesive layer progressively extended towards the asphalt layer's side along the direction of maximum principal stress. This extension primarily initiated at the interface, leading to the accumulation of damage. As the damage reached a critical threshold, interface debonding commenced. A comparative evaluation of the simulation data with the experimental findings is summarized in Table 5.

Table 5. Comparison of maximum load–displacement data of interlayer model with experiment.

Method	Maximum Load/N	Displacement/mm	Load Error/%	Displacement Error/%
Experiment	5589.130	0.713	0	0
VCCT	5450.182	0.504	2.4	29.1
XFEM–VCCT	5536.503	0.554	0.9	22.3
CZM	5771.36	0.713	3.2	0.1
XFEM–CZM	5544.17	0.688	0.8	0.3

At a simulation level, the failure processes across the different methods exhibited notable similarities. VCCT showed the highest deviation from the actual conditions, displaying a maximum load error of 24% and a displacement error of 29.1%. This disparity could be attributed to the neglect of the influence of adhesive layer thickness. On the other hand, CZM demonstrated a minimal displacement error, closely mirroring the experimentally derived failure displacement. However, its load error was comparatively higher, at 3.2%.

In contrast, the XFEM–CZM coupling method stood out, with a maximum load error of 0.8% and a maximum displacement error of 0.3%, providing the closest overall match to the experimental data. In practical terms, the XFEM–CZM coupling method not only accurately predicted the strength of Type I cracks between steel bridge deck asphalt paving layers but also effectively identified the initial occurrence of debonding at interfaces. Hence, the XFEM–CZM coupling method was strategically employed, offering a numerical forecast and a detailed crack propagation analysis of interlayer strength. It was notably compared with the CZM method, which exhibited a minimal load error, further underscoring the superior predictive capabilities of the XFEM–CZM coupling method.

4.2. Crack Extension and Interface Debonding Analysis

Under displacement-controlled conditions, the rightmost tip of the initial crack satisfied the maximum principal stress damage initiation criterion first. Subsequently, cracks extended through adjacent enriched elements, eventually penetrating the entire bonding layer, as depicted in Figure 9. STATUSXFEM in the figure represents the state of the expanding finite elements; these ranged between 0 and 1, where 1 signified complete damage and had no unit. When the radial displacement u reached 4.563×10^{-5} m, the stress value triggering the initiation of crack damage was reached. The crack started to extend towards the asphalt paving layer side and penetrated a single element. With a radial displacement of 2.531×10^{-4} m, the crack extended to the interface between the bonding layer and the asphalt paving layer. Subsequently, as displacement increased, strain energy accumulated at the interface, waiting for the interface strength to be reached before releasing the strain energy. This was followed by the propagation of cracks along the interface.

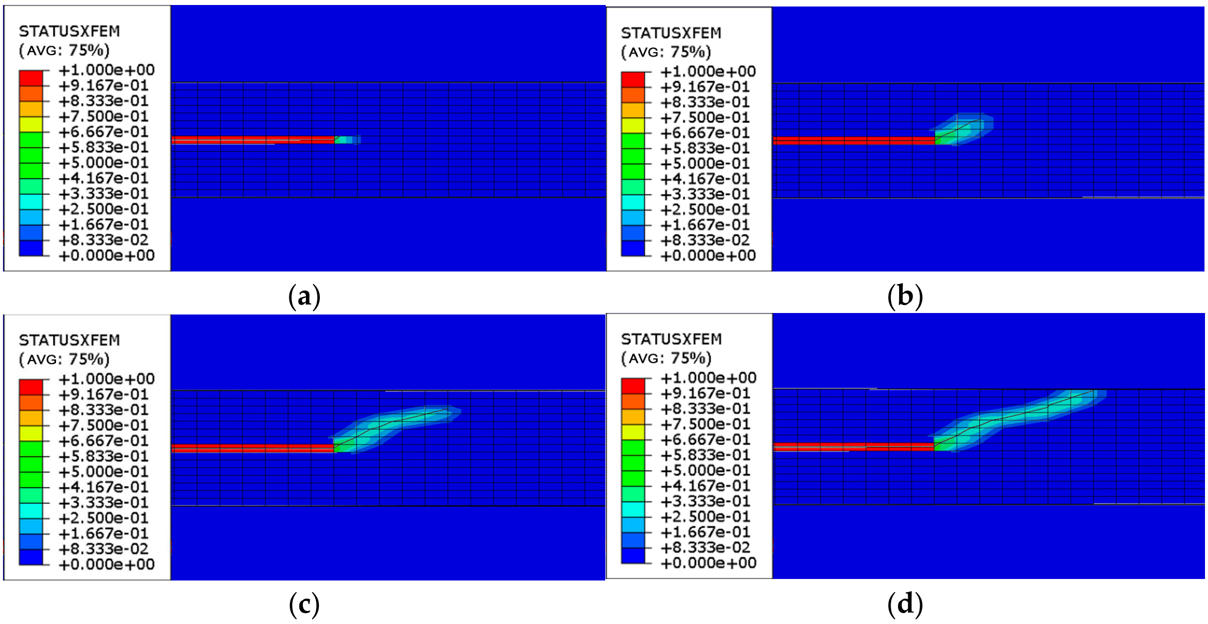

Figure 9. Initiation and propagation of cracks in the bonding layer: (**a**) crack initiation, $U = 4.563 \times 10^{-5}$ m; (**b**) crack propagation, $U = 7.766 \times 10^{-5}$ m; (**c**) crack propagation, $U = 1.313 \times 10^{-4}$ m; (**d**) crack reaches interface, $U = 2.531 \times 10^{-4}$ m.

For this study, the damage variable of cohesive elements was set at 0.99, signifying that cohesive elements failed and were deleted when the damage reached 0.99. This approach vividly reflected the interface failure process. The interface layering in the steel bridge deck–asphalt layer bonding model is illustrated in Figure 10. SDEG represents the stiffness degradation ratio of the elements; these ranged between 0 and 1, where 0 indicated an intact state and 1 indicated complete damage without units. At a radial displacement of 1.313×10^{-4} m, damage began to appear at the interface; however, the crack had not reached the interface. Under the influence of the stress field at the crack tip, damage accumulated at the interface, increasing as the crack approached. At a radial displacement of 2.537×10^{-4} m, the crack reached the interface, causing further damage accumulation at the interface. However, debonding had not occurred, resulting in interface layering. Subsequently, at a radial displacement of 6.789×10^{-4} m, partial debonding between the bonding layer and the asphalt paving layer occurred, leading to interface layering. Evidently, similar damage also arose at the interface between the steel bridge panel and the bonding layer, as depicted in Figure 11. This aligned with real-world scenarios, wherein after debonding, the steel plate remains partially bonded to the adhesive material while partially remaining smooth.

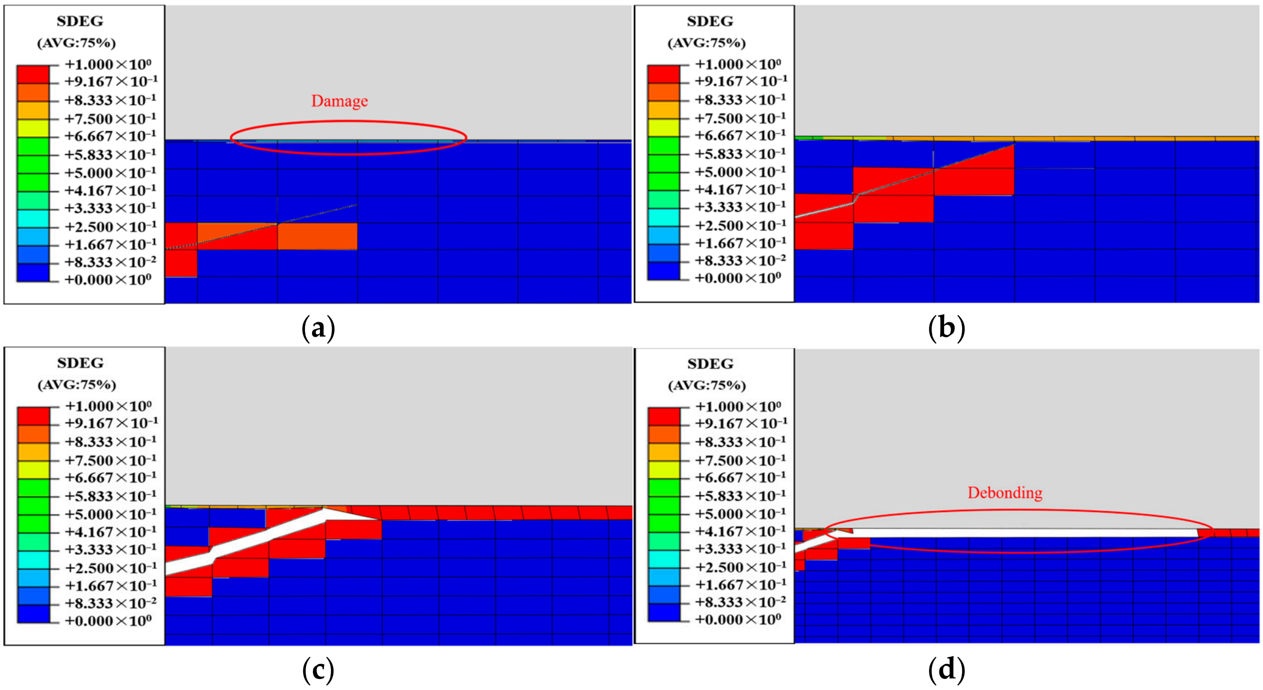

Figure 10. Interface layering process: (**a**) interface undamaged, U = 1.223 × 10^{-4} m; (**b**) interface damage occurs, U = 1.343 × 10^{-4} m; (**c**) interface damage occurs, U = 6.213 × 10^{-4} m; (**d**) interface debonding, U = 7.132 × 10^{-4} m.

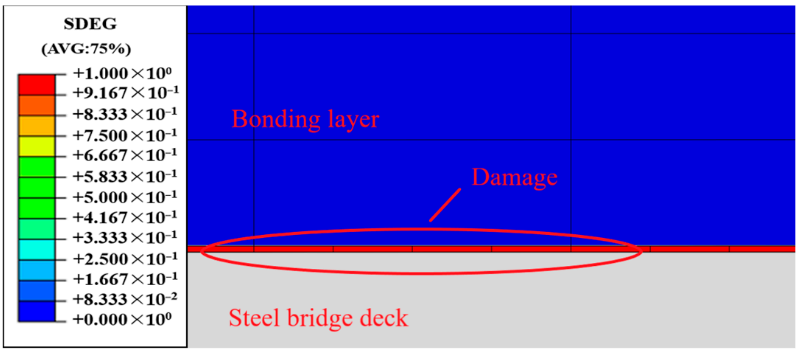

Figure 11. Damage at the interface between the steel plate and the bonding layer.

The entire failure process is visually apparent in Figure 12. Region A illustrates the extension of the crack towards the interface, while Region B depicts the accumulation of strain energy at the interface. Region C represents the point where the interface strength was reached and strain energy began to be released, triggering the expansion of interface cracks. For comparison, the cohesive zone model (CZM) method was also employed. The layering process simulated by the CZM method is illustrated in Figure 13, showing a highly similar failure process to XFEM–CZM. However, XFEM–CZM coupling provided a more intuitive representation of the complete process of the interface defect extension and the resultant layering.

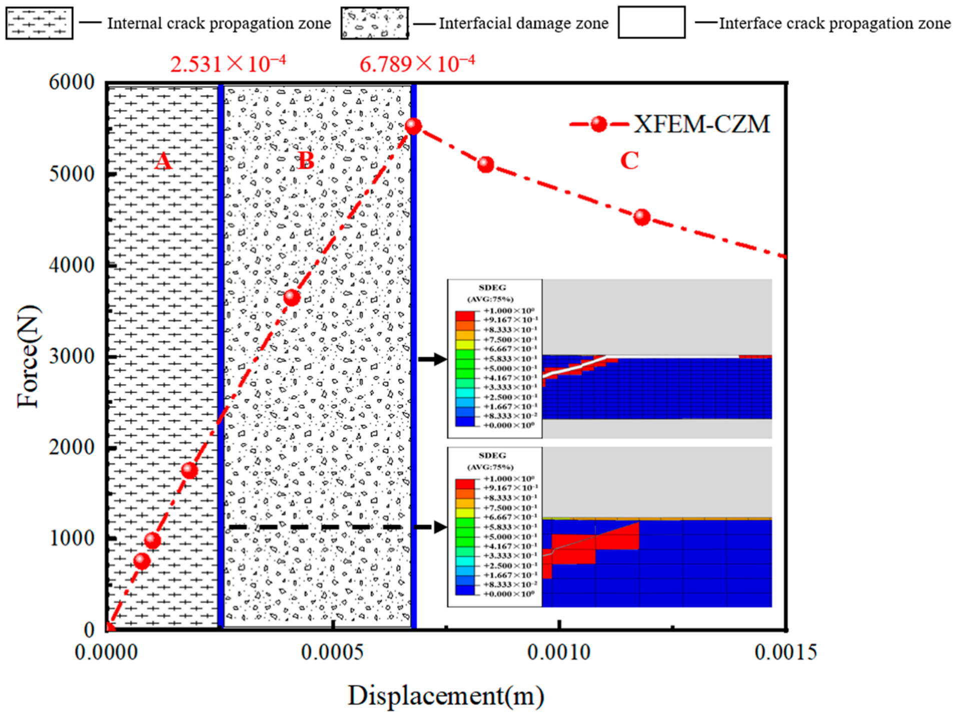

Figure 12. Load–displacement curve of double cantilever beam (DCB) under XFEM–CZM coupling.

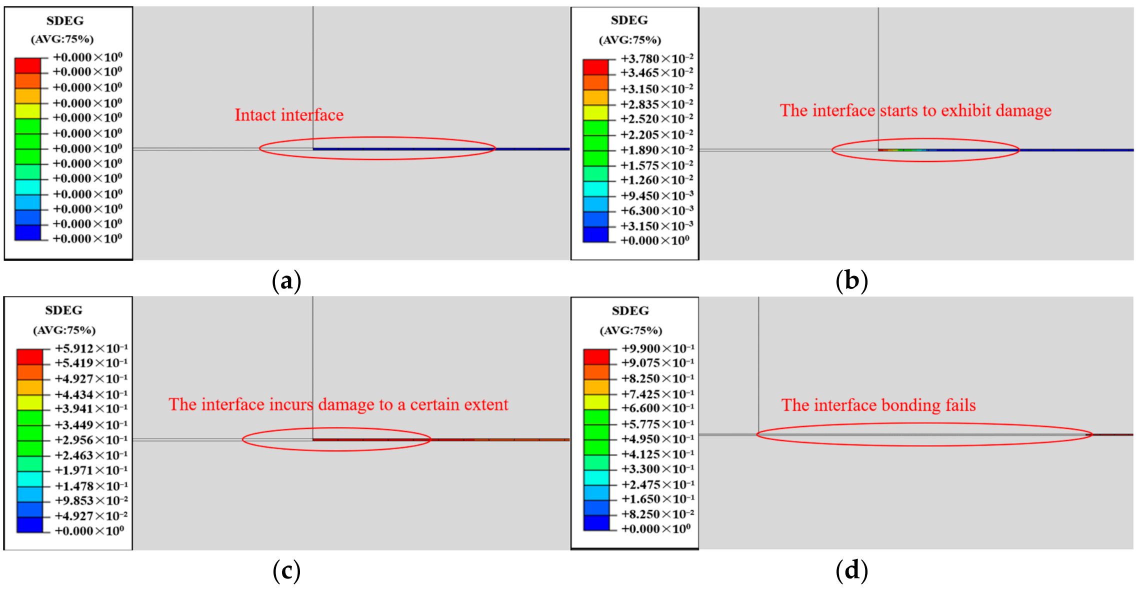

Figure 13. Interface layering process using the CZM method: (**a**) interface undamaged, U = 1.223 × 10^{-4} m; (**b**) interface damage occurs, U = 1.343 × 10^{-4} m; (**c**) interface damage occurs, U = 6.213 × 10^{-4} m; (**d**) interface debonding, U = 7.132 × 10^{-4} m.

4.3. Impact of Parameters

4.3.1. Influence of Initial Crack Length

In this study, the XFEM–CZM coupling model was employed to investigate the effects of different initial crack lengths on the propagation and strength of Type I cracks between a steel bridge deck and asphalt paving layers. The initial crack was positioned along the midthickness of the bonding layer on the left side, with lengths of 200 mm, 250 mm, 300 mm, 350 mm, and 400 mm. The results revealed that with an increasing crack length, the crack propagation path within the interlayer diminished, as illustrated in Figure 14.

When the crack lengths were 200 mm, 300 mm, and 400 mm, the cracks penetrated 15, 14, and 13 elements within the bonding layer, respectively.

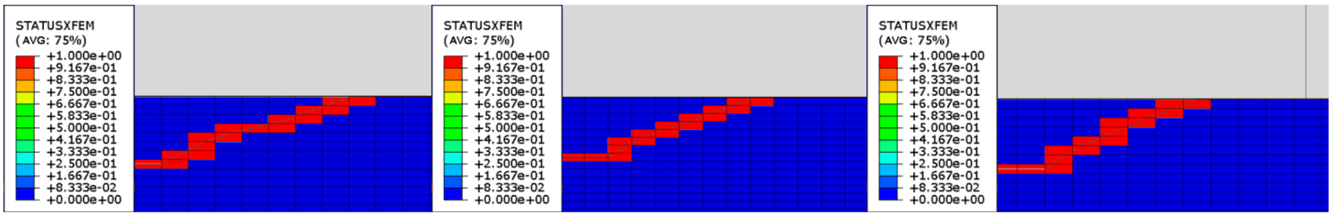

(**a**) 0.2 (**b**) 0.3 (**c**) 0.4

Figure 14. The crack growth path varied with the crack length.

From Figure 15a, it is evident that the bonding strength between the steel bridge panel and asphalt paving layer decreased as the initial crack length increased. Conversely, the failure displacement rose with an increasing crack length. This behavior was attributed to the more pronounced stress concentration effect at the crack tip with longer initial crack lengths, resulting in reduced structural strength. The increase in failure displacement was due to the higher elastic strain energy stored within the longer cracks. Consequently, longer cracks required more significant displacement to release the stored energy, enabling crack propagation and eventual failure. Figure 15b presents the computed load–displacement curve using the CZM method, showing a close resemblance to the XFEM–CZM coupling approach in terms of the maximum load and failure displacement. Figure 16 displays the predicted curves of strength and failure displacement obtained through simulation.

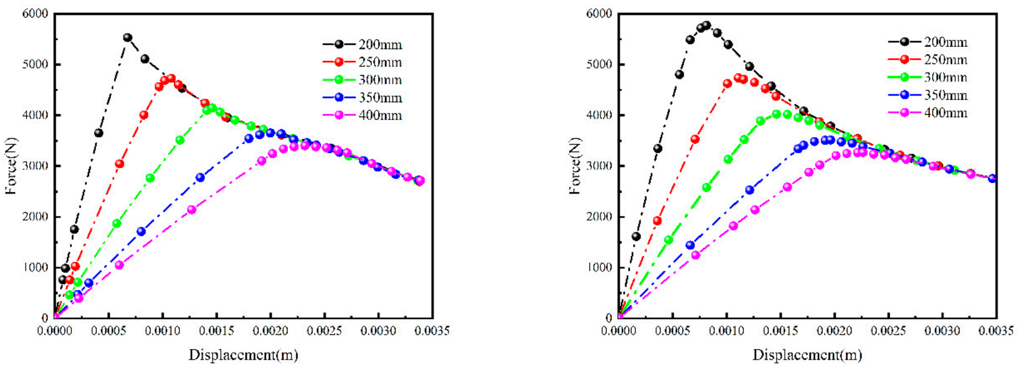

(**a**) XFEM–CZM (**b**) CZM

Figure 15. Variations in load–displacement curves with crack length.

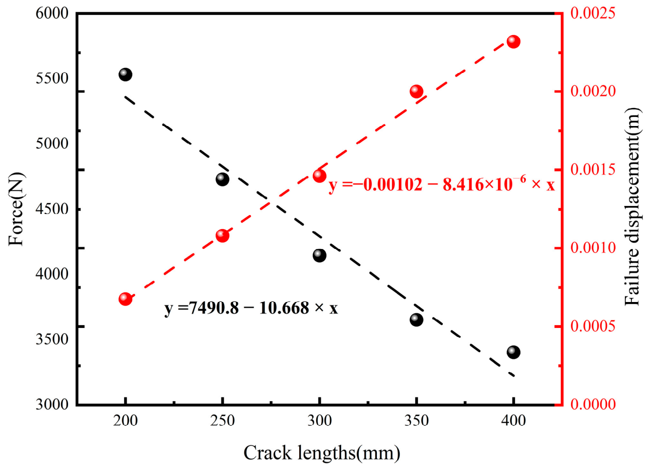

Figure 16. Strength and Failure Displacement Prediction Curves for Different Crack Lengths.

4.3.2. Effect of Interface Parameters

Interface stiffness and interface strength are two critical parameters in the cohesive zone model. In this section, we investigate the impact of these parameters on the propagation of Type I cracks between the steel bridge deck and asphalt paving layers as well as the strength prediction.

(1) Influence of Interface Stiffness

To explore the effects of different interface stiffness values on crack propagation and interface strength between a steel bridge deck and asphalt paving layers, simulations were conducted using interface stiffness values of 3.069×10^{11}, 4.069×10^{11}, 5.069×10^{11}, 6.069×10^{11}, and 7.069×10^{11} N/mm^3. The results demonstrated that as interface stiffness increased, the crack propagation path within the bonding layer expanded, as depicted in Figure 17. Specifically, when the stiffness was 3.069×10^{11} N/mm^3, the crack traversed 14 elements to reach the interface between the bonding and asphalt layers. However, for stiffness values of 5.069×10^{11} and 7.069×10^{11} N/mm^3, the crack penetrated 15 elements and the penetration length increased. The load–displacement curves for a steel bridge deck and asphalt paving layer with varying stiffness values are shown in Figure 18a. Figure 18b provides a comparison with the results obtained through the cohesive method.

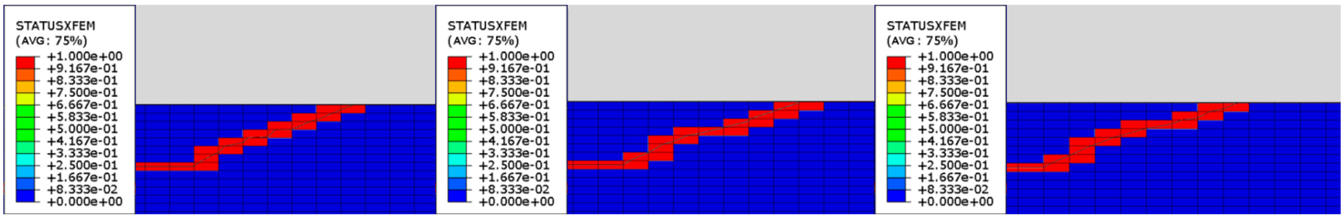

(**a**) 3.069×10^{11} (**b**) 4.069×10^{11} (**c**) 5.069×10^{11}

Figure 17. Variations in crack growth paths with interface stiffness.

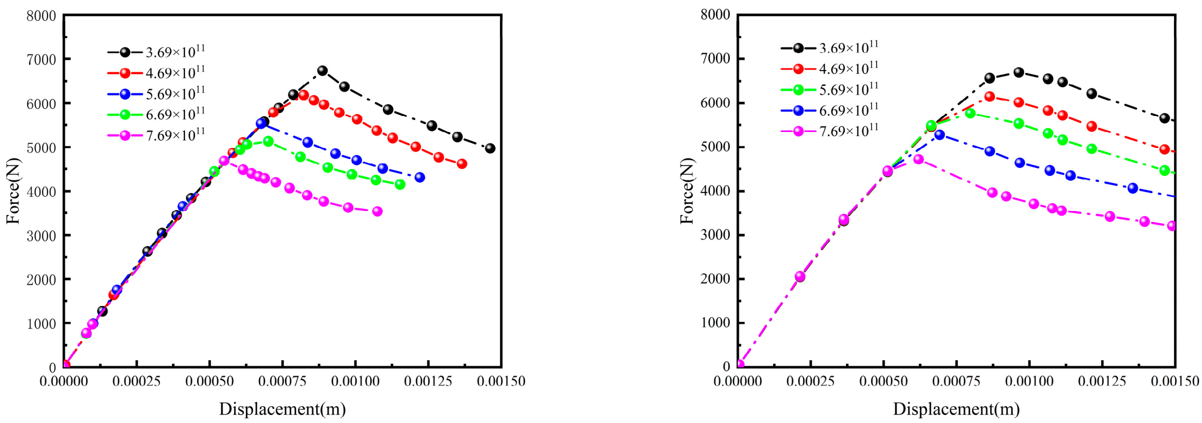

(**a**) XFEM–CZM (**b**) CZM

Figure 18. Variations in load–displacement curves with interface stiffness.

The outcomes revealed that both strength and failure displacement decreased as interface stiffness increased. This behavior could be attributed to the potential stress concentration near the interface due to elevated stiffness. Consequently, materials near the interface could experience higher stress levels, leading to a reduction in the interlayer bonding strength. The analysis indicated that interface stiffness values between 5.069×10^{11} and 6.069×10^{11} N/mm^3 yielded a good agreement with the actual strength values and improved the computational convergence. Therefore, when simulating the propagation of Type I cracks between a steel bridge deck and asphalt paving layers, an interface stiffness value in the range of 5.069×10^{11} to 6.069×10^{11} N/mm^3 is recommended. Figure 19 depicts the predicted curves of strength and failure displacement, revealing a notable linear relationship between them.

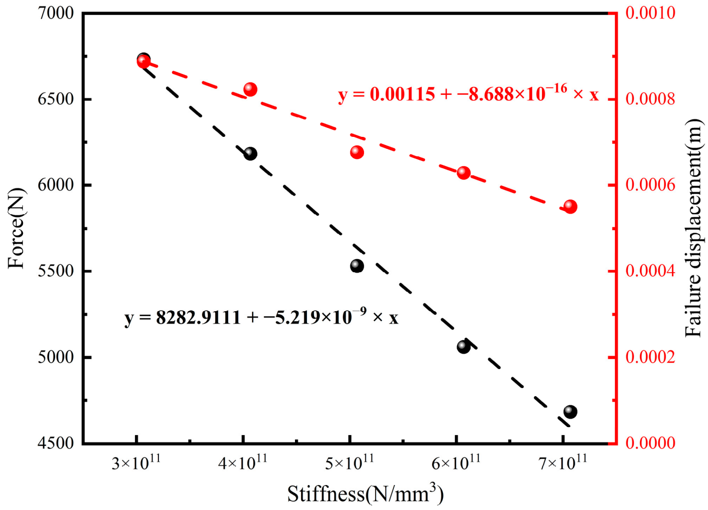

Figure 19. Strength and Failure Displacement Prediction Curves for Different Interface Stiffness.

(2) Influence of Interface Strength

To investigate the effects of different interface strength values on crack propagation between layers and the predicted interface strength, the interface strength was represented by σ. Specifically, 0.5σ signified half of the interface strength. Simulations were conducted using interface strength values of 0.5σ, 0.8σ, 1σ, 1.5σ, and 3σ. The findings revealed that changes in interface strength had minimal impact on crack propagation paths. As the strength increased, the variations in the crack propagation paths became negligible. When transitioning from 0.5σ to 3σ, the crack consistently penetrated 15 elements, as shown in Figure 20.

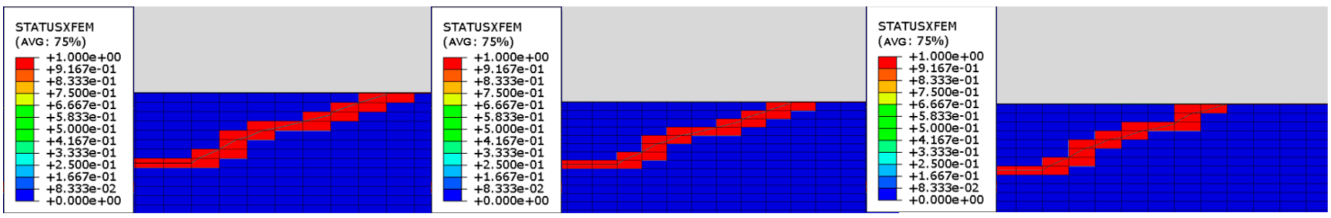

(**a**) 0.5σ (**b**) 1.0σ (**c**) 3σ

Figure 20. Variations in crack propagation paths with interface strength.

Clear effects on the load–displacement curves were observed, as demonstrated in Figure 21a, with a comparison to the CZM method shown in Figure 21b. When the interface strength increased from 1σ to 3σ, an increase of 95.8% in interface strength was accompanied by a 77.3% increase in the corresponding failure displacement. Additionally, failure displacement underwent significant augmentation. Thus, enhancing the interface strength notably elevated the interlayer bonding strength in the steel bridge deck and asphalt paving layers, enhancing structural reliability. Figure 22 illustrates the predicted curves of strength and failure displacement.

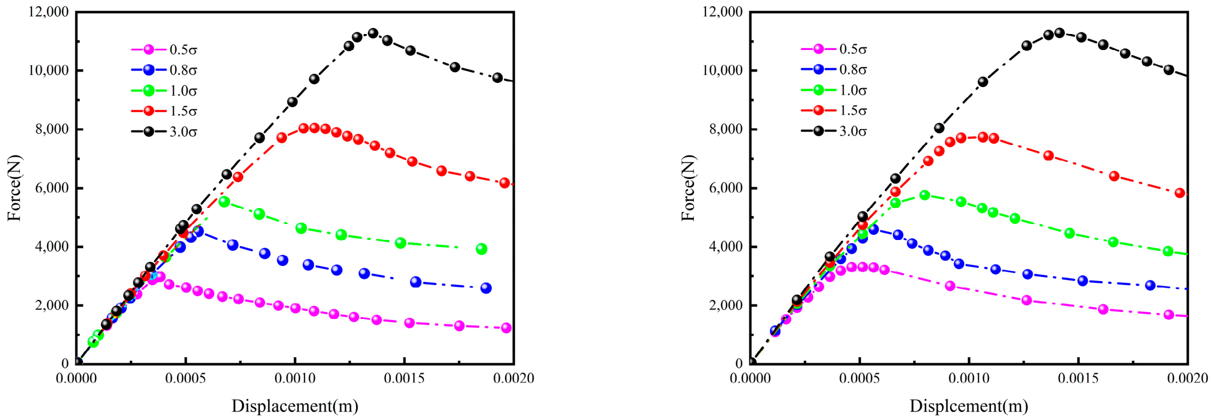

(**a**) XFEM–CZM (**b**) CZM

Figure 21. Variations in load–displacement curves with interface strength.

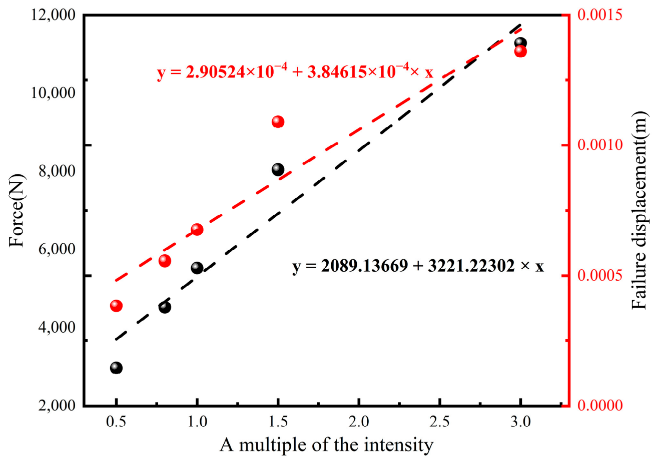

Figure 22. Strength and Failure Displacement Prediction Curves for Different Interface Strengths.

4.3.3. Influence of Bonding Layer Thickness

Based on practical engineering experience, the thickness of the bonding layer also significantly influences the interlayer bonding strength. To explore the effects of different bonding layer thicknesses on interlayer strength, simulations were conducted using bonding layers of 0.8, 1.0, 1.2, 1.4, and 1.6 mm thickness for Type I crack propagation. The results indicated that with an increasing bonding layer thickness, the crack propagation path within the bonding layer gradually enlarged. When the thickness was 0.8 mm, the crack penetrated 13 elements. However, as the thickness increased to 1.6 mm, the crack extended through 17 elements, as shown in Figure 23.

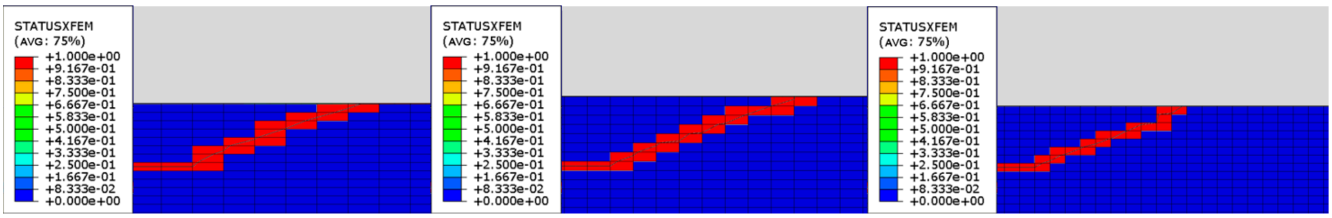

(**a**) 0.8 mm (**b**) 1.2 mm (**c**) 1.6 mm

Figure 23. Variations in crack propagation paths with bonding layer thickness.

Furthermore, the thickness increase also notably affected the load–displacement curves, as depicted in Figure 24a, with a comparison to the CZM method shown in

Figure 24b. The graphs illustrate a trend where the bonding layer strength initially increased and then decreased, as depicted in Figure 25. When the thickness increased from 0.8 mm to 1 mm, the interlayer strength improved, while a decrease in the interlayer strength occurred during the transition from 1 mm to 1.6 mm. Consequently, for optimal structural integrity during pavement construction, it is advisable to control the bonding layer thickness to enhance overall strength while avoiding excessive thickness. A recommended thickness of around 1 mm is suggested. When the adhesive layer is too thin, it fails to provide a sufficient bonding area, thereby lacking the required adhesive strength and weakening the bonding effect between materials. On the other hand, when the adhesive layer is too thick, internal stress concentration may occur, leading to the premature failure of the adhesive layer.

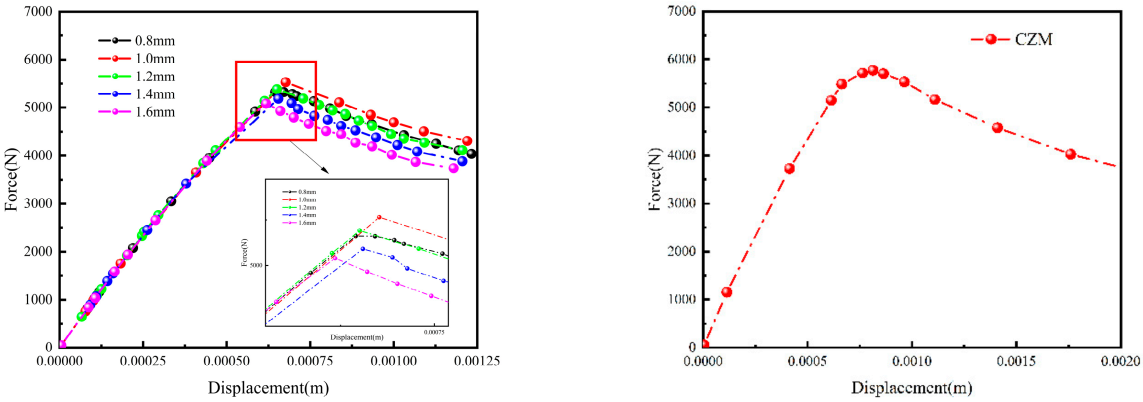

(**a**) XFEM–CZM (**b**) CZM

Figure 24. Variations in load–displacement curves with bonding layer thickness.

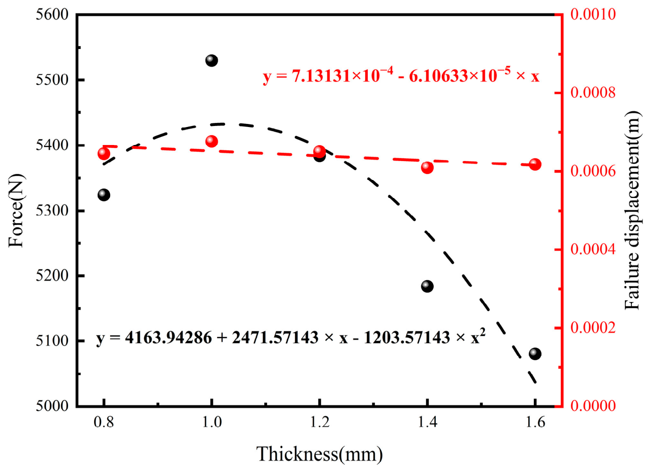

Figure 25. Strength and Failure Displacement Prediction Curves for Different Bond Layer Thicknesses.

4.3.4. Significance Analysis

An analysis of variance (ANOVA) was performed for different parameters to assess the significance of their effects on strength and failure displacement. This was achieved by analyzing the values of p and F. In significance analyses, the p-value holds crucial importance. When p is greater than 0.05, it signifies non-significance and when p is less than 0.05, it indicates significance; when p is less than 0.01, it is highly significant and when p is less than 0.001, it is extremely significant.

From the p-values presented in Figure 26, it can be observed that the significance order for strength and failure displacement was as follows: interface stiffness > crack length > interface strength > bonding layer thickness. Therefore, the results highlighted that changes in interface stiffness had the most substantial impact on strength and failure displacement. In areas where Mode I cracks are likely to occur, appropriately adjusting the interface stiffness may reduce the likelihood of crack formation.

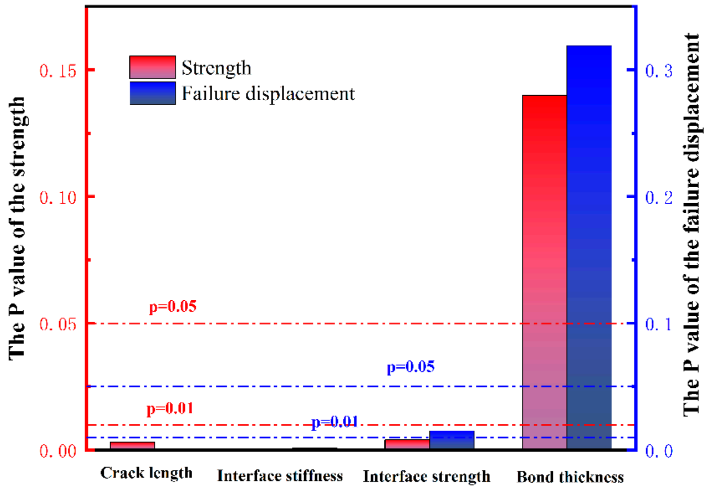

Figure 26. Significance Analysis of Different Parameters.

5. Conclusions

This study introduced a novel XFEM–CZM coupling method to analyze Type I cracking between steel plates and asphalt layers and demonstrated its effectiveness in predicting the failure strength and displacement of interlayer Type I cracks. The summarized key findings are as follows:

1. Cracks originating within the bonding layer propagated in the direction of the maximum principal stress until they reached the asphalt–bonding layer interface, resulting in interface damage and the occurrence of layering. Similar interface damage was observed between the bonding layer and the steel bridge deck. As displacement loads increased, various layering phenomena manifested at these interfaces.
2. Longer crack lengths within the layer led to reduced crack propagation, resulting in diminished strength and increased failure displacement. Increased interfacial stiffness widened the crack propagation path within the layer, consequently reducing strength and augmenting failure displacement. Although the interfacial strength exhibited a minor influence on the crack propagation path, it significantly impacted overall strength and interlayer failure displacement.
3. It is worth noting that interface stiffness and strength had minimal effects on the crack propagation path within the layer, but exerted a significant influence on the interlayer bonding strength. Enhanced stiffness diminished the bonding layer strength and failure displacement, while an elevated interface strength fortified the bonding layer strength and augmented failure displacement.
4. Variations in the thickness of the bonding layer affected the crack propagation path within the layer. An initial increase in thickness enhanced the bonding strength, but subsequent increments resulted in reduced strength. Our analysis recommended an optimal bonding layer thickness of approximately 1 mm to achieve a higher strength.
5. A significance analysis underscored that changes in interface stiffness had the most substantial impact on interlayer strength and failure displacement, followed by the influence of the crack length, interface strength, and bonding layer thickness. These findings shed light on the intricate interplay of parameters that influence crack propagation and interlayer bonding behavior.

Author Contributions: Conceptualization, C.Z. and H.W.; Methodology, C.Z. and H.W.; Software, C.Z.; Validation, C.Z. and W.L.; Resources, H.W.; Writing—original draft, C.Z.; Writing—review & editing, H.W.; Visualization, W.L. All authors have read and agreed to the published version of the manuscript.

Funding: This research received no external funding.

Institutional Review Board Statement: Not applicable.

Informed Consent Statement: Not applicable.

Data Availability Statement: Data are contained within the article.

Conflicts of Interest: The authors declare no conflict of interest.

References

1. Wang, H.; Li, G. Study of factors influencing gussasphalt mixture performance. *Constr. Build. Mater.* **2015**, *101*, 193–200. [CrossRef]
2. Ma, Y.; Wang, H.; Zhao, K.; Yan, L.; Yang, D. Study of a Modified Time Hardening Model for the Creep Consolidation Effect of Asphalt Mixtures. *Materials* **2022**, *15*, 2710. [PubMed]
3. Du, H.; Ni, F.; Ma, X. Crack resistance evaluation for In-service asphalt pavements by using SCB tests of layer-core samples. *J. Mater. Civ. Eng.* **2021**, *33*, 04020418. [CrossRef]
4. Zhang, M.; Hao, P.; Li, Y. Interfacial adhesive property in "asphalt mixture-PMA copolymer-steel plate" system: Experimental and molecular dynamics simulation. *Constr. Build. Mater.* **2021**, *281*, 122529.
5. Liu, Y.; Qian, Z.; Gong, M.; Huang, Q.; Ren, H. Inter-layer residual stress analysis of steel bridge deck pavement during gussasphalt pavement paving. *Constr. Build. Mater.* **2022**, *324*, 126624. [CrossRef]
6. Xue, C.; Wan, Y.; Wang, H. Mechanics Property Analysis for A New Steel Bridge Deck Pavement with UTAC—UHPC. *For. Eng.* **2020**, *36*, 76–84+93.
7. Liu, Y.; Qian, Z.; Yin, Y.; Ren, H. Investigation on inter-layer Behaviors of a Double-Layered Heterogeneous Asphalt Pavement Structure for Steel Bridge Deck. *J. Mater. Civ. Eng.* **2022**, *34*, 04022062. [CrossRef]
8. Jin, W.; Zhao, Y.; Wang, W.; He, F. Performance evaluation and optimization of waterproof adhesive layer for concrete bridge deck in seasonal frozen region using AHP. *Adv. Mater. Sci. Eng.* **2021**, *2021*, 5555535. [CrossRef]
9. Fu, J.; Shen, A.; Yuan, Z. Properties of Different Waterproof Bonding Layer Systems for Cement Concrete Bridge Deck Pavement. *Coatings* **2022**, *12*, 308. [CrossRef]
10. Zhang, M.; Hao, P.; Men, G.; Liu, N.; Yuan, G. Research on the compatibility of waterproof layer materials and asphalt mixture for steel bridge deck. *Constr. Build. Mater.* **2021**, *269*, 121346. [CrossRef]
11. Xu, Y.; Lv, X.; Ma, C.; Liang, F.; Qi, J.; Chou, Z.; Xu, S. Shear Fatigue Performance of Epoxy Resin Waterproof Adhesive Layer on Steel Bridge Deck Pavement. *Front. Mater.* **2021**, *7*, 618073. [CrossRef]
12. Ai, C.; Huang, H.; Rahman, A.; An, S. Establishment of a new approach to optimized selection of steel bridge deck waterproof bonding materials composite system. *Constr. Build. Mater.* **2020**, *264*, 120269. [CrossRef]
13. Chen, W.; Hui, B.; Rahman, A. Inter-layer Shear Characteristics of Bridge Deck Pavement through Experimental and Numerical Analysis. *Materials* **2022**, *15*, 7001. [CrossRef] [PubMed]
14. Xu, J.; Li, N.; Xu, T. Temperature changes of interlaminar bonding layer in different seasons and effects on mechanical properties of asphalt pavement. *Int. J. Pavement Res. Technol.* **2022**, *15*, 589–605. [CrossRef]
15. Zhang, W.; Li, Q.; Wang, J.; Meng, Y.; Zhou, Z. Aging Behavior of High-Viscosity Modified Asphalt Binder Based on Infrared Spectrum Test. *Materials* **2022**, *15*, 2778. [CrossRef]
16. Ma, X.; Kan, J.; Liu, S.; Tu, M.; Wang, D. Investigation of the Effect of Filler on Cohesive Bond Strength of Asphalt Mastic Using Binder Bond Strength (BBS) Test. *Coatings* **2023**, *13*, 1001. [CrossRef]
17. Chen, Z.; Xu, W.; Zhao, J.; An, L.; Wang, F.; Du, Z.; Chen, Q. Experimental Study of the Factors Influencing the Performance of the Bonding Interface between Epoxy Asphalt Concrete Pavement and a Steel Bridge Deck. *Buildings* **2022**, *12*, 477. [CrossRef]
18. Liu, Y.; Qian, Z.; Zheng, D.; Zhang, M. Interlaminar thermal effect analysis of steel bridge deck pavement during gussasphalt mixture paving. *Int. J. Pavement Eng.* **2019**, *20*, 1323–1335. [CrossRef]
19. Graczyk, M.; Zbiciak, A.; Michalczyk, R.; Kowalewski, Ł. Numerical modelling of bubbles formation in the bridge asphalt pavement under gas pressure impact. *Transp. Res. Procedia* **2016**, *14*, 3925–3934. [CrossRef]
20. Nie, W.; Wang, D.; Sun, Y.; Xu, W.; Xiao, X. Integrated design of structure and material of epoxy asphalt mixture used in steel bridge deck pavement. *Buildings* **2021**, *12*, 9. [CrossRef]
21. Yuya, W.; Yasushi, T.; Futoshi, K.; Kazuhiro, W. Evaluation of the Effect of Interlayer Bonding Condition on the Deterioration of Asphalt Pavement. *Transp. Res. Rec.* **2023**, *2677*, 03611981231153649. [CrossRef]
22. De Santis, Y.; Pasca, D.P.; Aloisio, A.; Stenstad, A.; Mahnert, K.C. Experimental, analytical and numerical investigation on the capacity of composite glulam beams with holes. *Eng. Struct.* **2023**, *285*, 115995. [CrossRef]
23. Koord, J.; Völkerink, O.; Petersen, E.; Hühne, C. Effect of low temperature on mode I and mode II interlaminar fracture toughness of CFRP-steel hybrid laminates. *Compos. Part B Eng.* **2023**, *262*, 110773. [CrossRef]

24. Yao, X.; Li, C.; Xu, T. Interfacial adhesive behaviors between SBS modified bitumen and aggregate using molecular dynamics simulation. *Surf. Interfaces* **2022**, *33*, 102245. [CrossRef]
25. Zhou, W.; Zhang, C.; Gan, S. Crack propagation analysis and strength prediction of glued joints based on XFEM-CZM coupling method. *J. Beijing Univ. Aeronaut. Astronaut.* **2020**, *46*, 2121–2130.
26. Feng, W.; Xu, H.; Yu, H.; Li, M. Adhesive damage and defect analysis of scarf-repaired composite by combining extended finite element method and cohesive zone model. *J. Compos.* **2018**, *35*, 1354–1360.
27. Belytschko, T.; Black, T. Elastic crack growth in finite elements with minimal remeshing. *Int. J. Numer. Methods Eng.* **1999**, *45*, 601–620. [CrossRef]
28. Moës, N.; Dolbow, J.; Belytschko, T. A finite element method for crack growth without remeshing. *Int. J. Numer. Methods Eng.* **1999**, *46*, 131–150. [CrossRef]
29. Zhuo, Z. *Extended Finite Element Method*; Tsinghua University Press: Beijing, China, 2012; pp. 35–36.
30. Melenk, J.M.; Babuška, I. The partition of unity finite element method: Basic theory and applications. *Comput. Methods Appl. Mech. Eng.* **1996**, *139*, 289–314. [CrossRef]
31. Gao, L.; Deng, X.; Zhang, Y.; Ji, X.; Li, Q. Fracture parameters and cracking propagation of cold recycled mixture considering material heterogeneity based on extended finite element method. *Materials* **2021**, *14*, 1993. [CrossRef]
32. Heidari-Rarani, M.; Sayedain, M. Finite element modeling strategies for 2D and 3D delamination propagation in composite DCB specimens using VCCT, CZM and XFEM approaches. *Theor. Appl. Fract. Mech.* **2019**, *103*, 102246. [CrossRef]
33. Wu, S. Study on the Interface Characteristics of Steel Deck Pavement with Engineered Cementitious Composites. Ph.D. Thesis, Southeast University, Dhaka, Bangladesh, 2019.
34. Qian, Z.; Liu, Y. Mechanical analysis of waterproof bonding layer on steel bridge deck under bridge-temperature-load coupling effect. *J. Southeast Univ. Nat. Sci. Ed.* **2012**, *42*, 729–733.